

# Stability of Accretion Shock around Cooling Filaments

Keshav Raghavan<sup>1</sup>, Han Aung<sup>1</sup>, Daisuke Nagai<sup>1,2\*</sup> et al.

<sup>1</sup>*Department of Physics, Yale University, New Haven, CT 06520, USA*

<sup>2</sup>*Department of Astronomy, Yale University, New Haven, CT 06520, USA*

29 October 2020

## ABSTRACT

**DN: This abstract provides a good opportunity for you to hone in your writing style, design, and basic writing skills.** The accretion mechanism of the gas onto filaments set the thermodynamic properties of the gas inside filament as well as the splashback and shock radius of the filament, the extent to which dark matter and filament gas exist. Radiative cooling can drive the filament shock inward by reducing the pressure support leading to collapse instead of an outgoing shock wave. The stability criterion can be presented by the effective polytropic index  $\gamma_{\text{eff}} > 1.25$  for monoatomic gas in filaments. We construct a self-similar solution for gas where the thermodynamic properties of the gas and shock are modeled consistently. In this paradigm, the profiles grow with time and radius in a simple power law, and the rescaled profiles only change with mass accretion rate. We calculate  $\gamma_{\text{eff}}$  of a self-similar filament for varying mass per unit length, mass accretion rate, and redshift and derive the regime where the filament shock is stable. Based on the self-similar solution and cooling mechanism, we predict the position of shock radius with respect to the splashback radius of the filament. Our work has implications on the size of the filament observable in the universe given the mass per unit length and mass accretion rate, and the thermodynamic properties of the filaments feeding massive halos which can affect galaxy formation physics.

**Key words:** hydrodynamics — miscellaneous — catalogs — surveys

## 1 INTRODUCTION

Filaments are the largest known structures in the universe, comprising the largest mass fraction of the cosmic web characterized by thread-like structures ranging up to 10 – 100Mpc (Doroshkevich 1970; Hahn et al. 2007; Cautun et al. 2014; Aung & Cohn 2016). Hydrodynamical cosmological simulations predict that the bulk of missing baryons in the universe reside in the form of warm-hot intergalactic medium (WHIM) residing in the cosmic web filaments (Cen & Ostriker 1999; Davé et al. 2001; Bregman 2007). Recent microwave and X-ray observations have detected some of the missing baryons in the universe (Planck Collaboration et al. 2013; Akamatsu et al. 2017; Hernández-Monteagudo et al. 2015; Nicastro et al. 2018; Tanimura et al. 2019; de Graaff et al. 2019; Lim et al. 2020). Upcoming microwave and X-ray missions, such as S-DIOS, Athena, Lynx, Simons Observatoary, CMB-S4 will have significantly improved that should help improve detection and characterization of the thermodynamic and chemical properties of WHIM.

The secondary mass accretion model can predict the profile and boundary of the halos and filaments and can serve as a foundation in constructing their physical model.

The self-similar model has been used to model collisionless dark matter in a spherical, cylindrical and planar symmetry corresponding to halos, filaments, and sheets in cosmic web by using mass, mass per unit length, and mass per area respectively (Fillmore & Goldreich 1984, hereafter FG84) as well as and collisional gas for spherical symmetry (Bertschinger 1985, hereafter B85). As dark matter shells infall from turnaround radius, they move radially inward to the halo center, splashback out, and is halted at ‘splashback’ radius, which is located at the radius smaller than the initial turnaround radius due to the growth of the potential well. In absence of cooling, the gas is bounded by an accretion shock for collisional gas, where cool-warm gas gets shock heated when infalling onto a hot halo. The splashback and shock radii of spherical halos coincide regardless of the mass accretion rate or baryon fraction if the polytropic index is kept at  $\gamma = 5/3$  (Shi 2016b, hereafter XS16). The model predicts the location of splashback radius of the halo and the dependence on the mass accretion rate in N-body simulations successfully (Adhikari et al. 2014).

The stability criterion of gas shock is important in studying the filament formation mechanism and galaxy formation physics. Based on their conclusions, cooling can affect the lowest mass large scale filament webs connecting galaxy clusters down to small scale filaments connecting fil-

\* E-mail: daisuke.nagai@yale.edu

aments. The filamentary gas streams form the main channel for the gas accretion of high-redshift star forming galaxies (Kereš et al. 2005; Dekel et al. 2009; Ceverino et al. 2010) as well as low redshift galaxy clusters (Zinger et al. 2016). However, radiative cooling can significantly impact the shock as it reduces the pressure support and leads to instability and the inward collapse of shock radius for smaller mass ( $M \lesssim 10^{11} M_\odot$ ) and/or high redshift ( $z \gtrsim 2$ ) halos (Birnbom & Dekel 2003). A similar criterion for the stability of the filament shock implies that gas stream feeding the shock of  $10^{11} M_\odot \lesssim M_{\text{halo}} \lesssim 10^{13} M_\odot$  at  $z = 3$  and  $10^{12} M_\odot \lesssim M_{\text{halo}} \lesssim 10^{15} M_\odot$  at  $z = 0$  are not shock heated (Birnbom et al. 2016, hereafter B16). However, the previous stability limit of shock in B16 is derived assuming the dark matter profile from a self-similar solution without the location of shock radius and the thermodynamic properties of gas consistently defined.

In this paper, we derive the self-similar solution of gas due to secondary accretion onto filaments and predict the location of the shock radius, following the infall of cylindrical symmetry used in FG84, and the collisional gas model in B85 and XS16, assuming monatomic gas  $\gamma = 5/3$  in Einstein-de Sitter universe,  $\Omega_m = 1$  and  $H_0 = 70 \text{ km/s/Mpc}$ . We calculate stability criterion for the filament shock in mass per unit length for filamentary shock, and its dependence on redshift and mass accretion rate, in the presence of cooling based on B16 in section 2.2, and summarize how the shock radius position will change if cooling is incorporated. We present the theoretical background reviewing relevant work in section 2. We present our results of self-similar shock in the presence of cooling in section 3. We discuss the caveats and various simplifying assumptions of our analytic model in section 4 and present our conclusions in section 5.

## 2 THEORETICAL FRAMEWORK

### 2.1 Secondary Accretion Model

We first summarize the secondary mass accretion onto filament described in FG84. A filament is modeled as an infinitely long cylindrical mass perturbation which is invariant under translation along or rotation about its axis. We assume an initial overdensity  $\Delta_i$  within the cylindrical radius  $R_i$  at time  $t_i$ , in an otherwise isotropic Einstein-de Sitter ( $\Omega_m = 1$ ) universe with background density

$$\rho_b = \rho_m = \frac{1}{6\pi G t^2}. \quad (1)$$

Due to the overdensity, the cylindrical shells of matter are halted and turned around when the expansion balances the gravitational attraction of the perturbation. When lengths are scaled by this turnaround radius  $r_{\text{ta}}(t)$ , the infall process becomes self-similar. Due to the continuous infall of cylindrical shells, the mass per unit length inside the turnaround radius of the filament,  $m$  grows as  $m \propto a^{s-1}$ .<sup>1</sup> Accordingly, the turnaround radius grows in time,  $r_{\text{ta}}(t) \propto t^\delta$ , where  $\delta = 2(1 + s/2)/3$ . The initial turnaround radius for cold

<sup>1</sup> Similar mass growth for halo uses  $m \propto a^s$  in FG84 and XS16, where the difference is attributable to the number of axes along which the Hubble flow transports mass, cf. FG84 eq. 12.

**Table 1.** Scaling relations: dimensional & nondimensional

Dimensional	Filament	Halo
$t$	$\xi = \ln(t/t_{\text{ita}})$	$\xi$
$r$	$\lambda = r/r_{\text{ta}}$	$\lambda$
$m$	$M(\lambda) = m / (\pi r_{\text{ta}}^2 \rho_b)$	$M(\lambda) = 3m / (4\pi \rho_b r_{\text{ta}}^3)$
$p$	$P(\lambda) = (t/r_{\text{ta}})^2 p / \rho_b$	$P(\lambda)$
$v$	$V(\lambda) = vt / r_{\text{ta}}$	$V(\lambda)$
$\rho$	$D(\lambda) = \rho / \rho_b$	$D(\lambda)$

matter is  $r_{\text{ita}} = 0.74 R_i \Delta_i^{-1}$  and initial turnaround time  $t_{\text{ita}} = 1.64 \Delta_i^{-3/2} t_i$ , where  $t = t_i$  is the initial cosmic time, i.e., the time when radiation and matter decouple (FG84, eqs. 13-14). The initial turnaround time ( $t_{\text{ita}}$ ) marks the moment of first collapse in our set-up, i.e. the time when the local density contrast between the cylinder and background grows to the point that the enclosed matter falls back in.

To achieve dimensionless self-similar forms, we rescale any physical quantities with the initial turnaround time ( $t_{\text{ita}}$ ), turnaround radius at observed time  $r_{\text{ta}}(t)$ , and the background density at observed time  $\rho_b(t)$ . The physical quantities of interest are time ( $t$ ), radius ( $r$ ), enclosed mass per unit length ( $m$ ), pressure of gas ( $p$ ), velocity ( $v$ ), and density ( $\rho$ ). We contrast the relations for filament used in our paper and those for halo in XS16<sup>2</sup> in Table (1). This effectively removes any time dependence for dimensionless quantities and achieves self-similar quantities.

For collisionless dark matter, the equation of motion is given by

$$\frac{d^2 r}{dt^2} = \frac{r}{9t^2} - \frac{2Gm}{r}, \quad (2)$$

where the first term is to remove double counting the background density.

The dimensionless equation of motion can then be written as

$$\frac{d^2 \lambda}{d\xi^2} + (2\delta - 1) \frac{d\lambda}{d\xi} + \delta(\delta - 1)\lambda = \frac{\lambda}{9} - \frac{M}{3} - \frac{P'}{D}. \quad (3)$$

Following the example of Bertschinger (1985) and Shi (2016a), we obtain the mass profile and trajectory via a method of convergent iterations. As dark matter is collisionless, infalling dark matter passes through the origin back and forth and there exists multiple shells of dark matter at each radius. The total mass at the radius  $\lambda$  is the sum of the mass of all dark matter shells at  $\lambda$ ,

$$M(\lambda) = \sum_i M_i = \sum_i (-1)^i M_{\text{ta}} \exp(-2s\xi_i/3), \quad (4)$$

where each shell, characterized by a fixed radial parameter  $\lambda$  at time  $\xi = \xi_i$ , has mass  $M_i$ . The alternating signs account for streams flowing out versus in, and the mass is scaled by the time since the individual shell crosses the turnaround radius,  $\exp(-2s\xi/3) \propto t^{-2s/3}$ . We begin with an initial guess

<sup>2</sup>  $m$  is mass instead of mass per unit length for a halo.

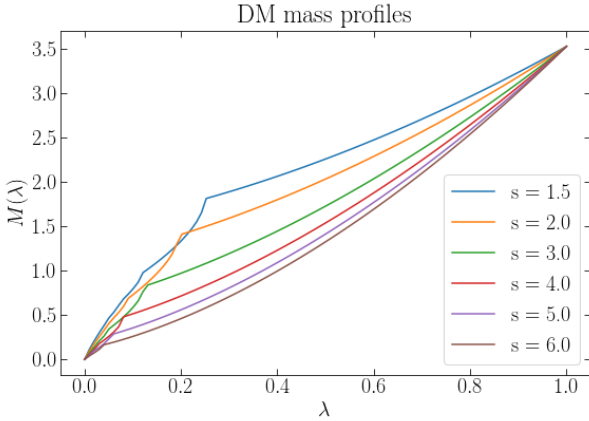


**Figure 1.** The dimensionless dark matter mass profiles found via the method of iterations for various mass accretion rates. The higher the mass accretion rate, the smaller the splashback radius where the mass profile slope shifts.

for the mass distribution,  $M_0(\lambda) = M_{\text{ta}}\lambda^{0.74}$  and numerically integrate the equation with the boundary condition of  $M(\lambda = 1) = M_{\text{ta}} = (1.39/0.74)^2$ , as calculated in FG84, and  $d\lambda/d\xi(\lambda = 1) = -\delta$ . Recall that  $r_{\text{ta}} \propto t^\delta$ , and hence the particle is falling inward. Then, using the resultant trajectory, we recalculate the mass distribution. The iteration of calculating the trajectory with the new mass profile and the mass distribution is then repeated until the difference in the mass profile differs by less than 1%. In this way we can generate the dark matter mass profiles in Fig. 1. The break in mass profile indicates the splashback radius of filament inside which multiple mass shells previously accreted contribute to the mass profile.

## 2.2 Cooling and Shock Stability

Radiative cooling plays a crucial role in the stability of the filament shock. The stability criterion is presented by whether the effective adiabatic index of gas during cooling is larger or smaller than a specific value (Birnbom & Dekel 2003, B16). The effective adiabatic index is given by

$$\gamma_{\text{eff}} = \left( \frac{\partial \ln p}{\partial \ln \rho} \right)_s = \frac{\rho}{p} \frac{dp/dt}{d\rho/dt} = \frac{\rho}{p} \frac{dp/dr}{d\rho/dr}, \quad (5)$$

for a parcel of gas under Lagrangian trajectory. We can relate the internal energy and temperature to the pressure and density using the ideal-gas law:

$$e = \frac{p}{(\gamma - 1)\rho}, \quad k_B T = \frac{\mu p}{N_A \rho}, \quad (6)$$

where  $\mu$  is the mean molecular weight and  $N_A$  is Avogadro's number. Using the first relation of eq. 6, the time derivative of pressure can be replaced by that of energy. The change in internal energy is given by the conversation of energy

$$\dot{e} = \frac{P\dot{\rho}}{\rho^2} - q, \quad (7)$$

where the left term describes work done by pressure and  $q = \rho\Lambda_{\text{cool}}(T, Z) = \rho(N_A\chi/\mu)^2\Lambda_{\text{mic}}(T, Z)$  encodes the cooling rate. Here,  $Z$  is the metallicity of the fluid, and  $\chi$  is the

number of electrons per particle, assuming primordial gas composition. The microscopic cooling function  $\Lambda_{\text{mic}}(T, Z)$  is obtained from the cooling tables in Sutherland & Dopita (1993).

Assuming mass continuity,

$$\left( \frac{\rho}{\dot{\rho}} \right)^{-1} = -2 \frac{v}{r}. \quad (8)$$

Combining the second equality in eq. 5 and eqs.6-8 results in

$$\gamma_{\text{eff}} = \gamma + \frac{1}{2} \frac{r}{v} \cdot \frac{\rho^2(\gamma - 1)}{p} \cdot \Lambda_{\text{cool}}(T, Z). \quad (9)$$

For the stability criteria of the shock, we consider a small displacement  $\delta r$  of the perturbed gas parcel within a small time frame  $\delta t$ . If the acceleration on this displacement is positive ( $\ddot{\delta r} > 0$ ), it is a stable outward motion, whereas the negative sign ( $\ddot{\delta r} < 0$ ) means inward collapsing motion. This is equivalent to determining the sign on jerk  $\ddot{r} \equiv \ddot{\delta r}/\delta t$ . The equation of motion is given by a hydrostatic assumption:

$$\ddot{r} = -\frac{1}{\rho} \nabla p - \frac{Gm}{r} = 0, \quad (10)$$

where  $m$  is the mass per unit length as a function of radius. Differentiating with respect to time, we obtain

$$\ddot{r} = \frac{1}{\rho^2} \dot{\rho} \nabla p - \frac{1}{\rho} \nabla \dot{p} + \frac{Gm}{r^2} \dot{r}, \quad (11)$$

where we exchange the spatial and time derivative of  $P$ .

Using the relation between spatial and time derivatives of pressure and density using eq. 6 and 9, and the fact that  $dP/dr < 0$  to counteract the gravity, the stability criterion can be written as

$$\gamma_{\text{eff}} > \frac{4\gamma}{2\gamma + 2}. \quad (12)$$

For detailed derivations, see B16. For  $\gamma = 5/3$  (ideal monatomic) this reduces to the condition  $\gamma_{\text{eff}} > 1.25$ .

By inferring the gas profile values from dark matter filament profile in Fillmore & Goldreich (1984), the result generally concludes that there will be no stable shock for filaments of  $M_{\text{fil}} \approx 10^{11} - 10^{13} M_\odot/\text{Mpc}$ . This filament mass range corresponds to virial temperature of around  $10^4 - 10^6 \text{K}$ , where the virial temperature is given by

$$k_B T \approx GM_{\text{fil}} m_p. \quad (13)$$

Around this temperature range, the cooling rate significantly increases due to hydrogen and helium line cooling, and the cooling time is shorter than the dynamical time. Outside this temperature range, there is no significant cooling assuming primordial gas composition.

## 3 RESULTS

### 3.1 Self-similar filaments

Following the secondary accretion model of filaments for dark matter as well as the accretion shock model for halos described in B85 and XS16, we will calculate the accretion shock radius of the filament. To locate the self-similar shock radius  $\lambda_{\text{sh}}$  (i.e., the ratio of shock radius and turnaround

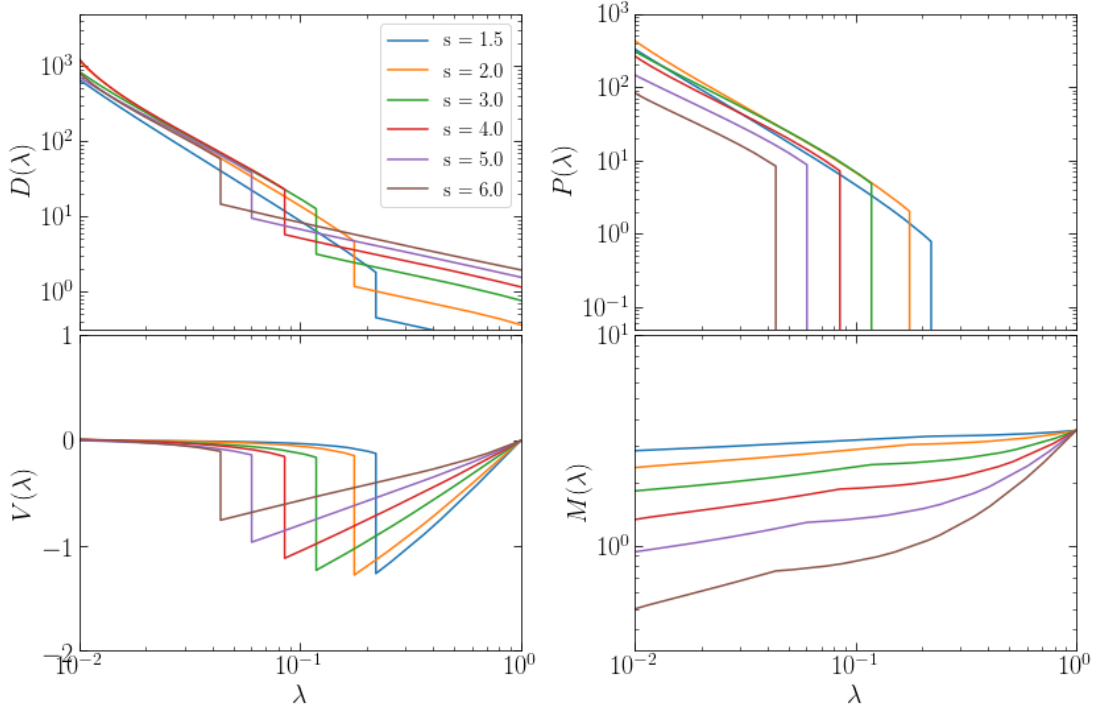


**Figure 2.** The dimensionless density, pressure, velocity and mass profiles for filaments at various mass accretion rates. Outside shock, pressure is assumed to be negligible. At shock radius, density, pressure, and velocity profiles are discontinuous.

radius is constant), we need to take into account the pressure of the gas. The self-similar shock has a velocity of  $\delta\lambda_{\text{sh}}$ , since  $r_{\text{ta}} \propto t^\delta$ . Assuming adiabatic gas flow, the governing equations for the gas motions are

$$\begin{aligned} \frac{d\rho}{dt} &= -\frac{\rho}{r} \frac{\partial}{\partial r}(rv), \\ \frac{dv}{dt} &= \frac{r}{9t^2} - \frac{1}{\rho} \frac{\partial p}{\partial r} - \frac{2Gm}{r}, \\ \frac{d}{dt}(p\rho^{-\gamma}) &= 0, \\ \frac{\partial m}{\partial r} &= 2\pi r\rho. \end{aligned} \quad (14)$$

Respectively, these are the continuity, Euler, adiabatic, and mass conservation equations. We assume the polytropic index of  $\gamma = 5/3$  throughout the paper. The eqs. (14) can be nondimensionalized according to the relations provided in Table 1. We then have a system of coupled ordinary differential equations in  $\lambda$  that may be solved with appropriate boundary conditions. Prior to shock, the gas is assumed to be pressureless, and we have  $P = 0$  and  $dP/dt = 0$ , in which case we ignore the adiabatic relation and the Euler equation reduces to Newton's third law. If there is a shock in the gas trajectory, the thermodynamic quantities are discontinuous across the shock and the behavior of the gas is given by the

jump conditions assuming normal shock (XS16):

$$\begin{aligned} V_2 &= \frac{\gamma-1}{\gamma+1} [V_1 - \lambda_{\text{sh}}\delta] + \lambda_{\text{sh}}\delta, \\ D_2 &= \frac{\gamma+1}{\gamma-1} D_1, \\ P_2 &= \frac{2}{\gamma+1} D_1 [V_1 - \lambda_{\text{sh}}\delta]^2, \\ M_2 &= M_1, \end{aligned} \quad (15)$$

where the jump is expressed in terms of the dimensionless quantities  $D, P, V, M$ , and the subscripts indicate pre-shock (1) and post-shock (2).

To solve for the gas trajectories and profiles, we specify the outer and inner boundary conditions. At  $\lambda = 1$ , we take  $P = 0, V = 0, M = M_{\text{ta}}$ . The density boundary condition is found by numerically calculating the slope  $M'(\lambda = 1)$  from the dark matter iterative solution (FG84). The inner boundary condition is  $V = 0$  at the origin. We then solve the equations numerically from  $\lambda = 1$  to  $\lambda_{\text{sh}}$ , apply shock jump conditions, and then solve from  $\lambda_{\text{sh}}$  to the origin. The shock radius is chosen such that it satisfies the interior boundary conditions  $V = 0$  and  $M \geq 0$  at the origin.<sup>3</sup>

Fig. 2 shows the resulting profile of gas for different mass accretion rates. Each of these filament density profiles has a profile of  $\rho \propto r^{-1.62}$  near the origin, with relatively small dependence on mass accretion rate. The pressure profile slope also exhibits independence on mass accretion rate.

<sup>3</sup> Since the profiles diverge at the origin, we are only able to integrate up to a small offset from the origin.

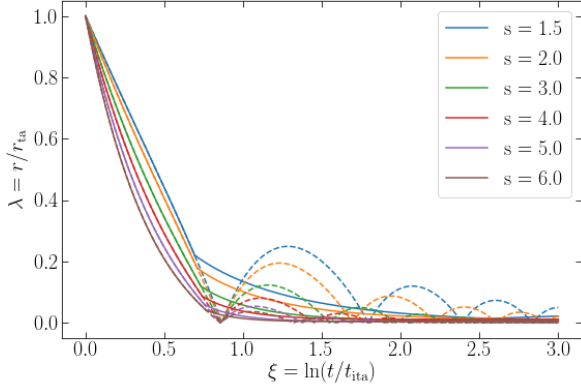


**Figure 3.** The trajectories for different mass accretion rates, iterated to 1 percent convergence. The gas trajectories are the same as DM until the shock, after which eqs. 14 are used. The second peaks in DM trajectories denote splashback radius, while the radius where gas trajectories diverge from DM denote shock radius. At any observed time, the two radii are similar.

This is similar to the dark matter density profile (FG84), where it is shown that the density profile slope of filament is independent of mass accretion rate, whereas the profile slopes of halos and sheets change with  $s$ . Similar to dark matter halo, for the larger mass accretion rate  $s$ , the potential well grows faster, and the shock radius would be smaller. The shock radius reaches maximum at  $r \approx 0.15r_{ta}$  when  $s \gtrsim 1$ .

Self-similar solution ceases to exist for  $s < 1$ . Since  $m \propto a^{s-1}$ ,  $s = 1$  represents the point where the mass per unit length is not growing even though there is overdensity perturbation. At this point, the decrease in mass per unit length due to the expansion of the universe along the filament axis is larger than the mass gained by the secondary accretion. Thus, in this paper, we focus on higher mass accretion rate regime where the stable solution exists.

We can obtain the trajectories of the infalling gas shell by integrating the velocity profile  $V(\lambda)$ . Fig. 3 shows the resulting gas trajectories and the comparison to the dark matter trajectories from section 2.1. Starting at turnaround radius  $\lambda = 1$  at time  $\xi = 0$ , the infalling gas and dark matter obey the same equations until the shock radius. At the shock radius, the kinetic energy of the gas is converted into thermal energy and slows down leading to an asymptotic trajectory toward  $\lambda = 0$  at large  $\xi$ . Dark matter shells, however, continue on its trajectory of infall into the center, and splashback outside after. The maximum radius dark matter reaches for the second turnaround defines the splashback radius of the filament. The dark matter then continues this process repeatedly, with each successive splashback radii becoming smaller and smaller. Note that the solutions for the filament begin to exhibit disparate behavior from those of the spherical halo given in Shi (2016b) for  $s \lesssim 2.5$ . Specifically, the successive maximum radius to which dark matter splashback shells starts to grow in physical units, but decreases when normalized with respect to the turnaround radius at the observed time, thus retaining self-similar solu-

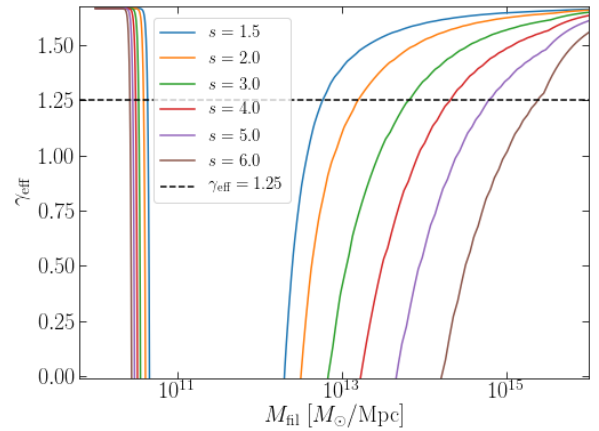


**Figure 4.**  $\gamma_{\text{eff}}$  values at  $r = r_{\text{sh}}^-$  for different mass accretion rates at redshift of 0.2. The dips are largely due to the peaks in the cooling function. Also plotted is the dashed horizontal line denoting the stability criterion from eq. 12. The upper bounds of instability regime increase with mass accretion rate, significantly increasing the gap.

tion for  $s > 1$ . The dark matter splashback and gas shock radii coincide for all mass accretion rates.

The dimensionless profiles calculated for the self-similar solutions can be converted to dimensional quantities using the relations given in Table 1, by specifying the background density  $\rho_b$ , and turnaround radius  $r_{ta}$ . Note that specifying  $\rho_b$  also specifies time  $t$  through eq. 1. For a given redshift, the background density of the Einstein-de Sitter universe can be obtained as  $\rho_b = \rho_{b,0}(1+z)^3$ . We can find the turnaround radius by asserting that the radius of the filament is the shock radius  $r_{sh} = R_{fil}$ , and the mass per unit length of the filament is the mass enclosed within the shock radius of the filament,  $M_{fil} = M(\lambda_{sh})\pi r_{ta}^2 \rho_b$ . Thus, specifying the mass per unit length and the redshift of the filament specifies all the scaling factors needed to convert dimensionless profiles to dimensional quantities in Table 1.

### 3.2 Effects of Cooling

We want to determine the shock stability of the post-shock gas at the shock radius given the radiative cooling by applying the stability criterion eq. 12 on the effective polytropic index  $\gamma_{\text{eff}}$ . Using eq. 9 and the profiles generated in section 3.1, we can calculate the  $\gamma_{\text{eff}}$  of the post-shock gas at the shock radius ( $r \rightarrow r_{sh}^-$ ) for given filament mass, redshift, and mass accretion rate. Since the gas at the shock radius is just accreted onto the filament, we assume primordial composition:  $\mu = 0.61\text{g/mol}$ ,  $Z = 0$ , and  $\chi = 1$ . Figures 4 and 5 show  $\gamma_{\text{eff}}$  of the post-shock gas at the shock radius as a function of  $M_{fil}$  with varying mass accretion rates at redshift 0 or varying redshifts with constant mass accretion rate  $s = 3$ .

We notice from Fig. 4 that, as we increase the mass accretion rate  $s$ , the mass stability gap grows. Note that this is equivalent to decreasing the initial mass perturbation exponent  $\epsilon = 1/s$ . The left intersection point between  $\gamma_{\text{eff}} = 1.25$  and the calculated curve corresponds roughly to



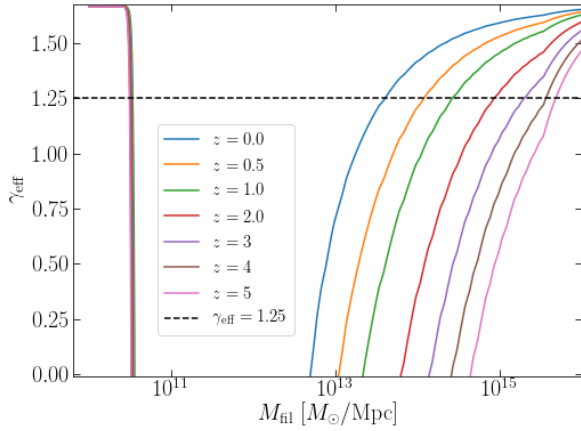


**Figure 5.** Same as Fig. 4, but for different redshifts with mass accretion rate of  $s = 3$ . As we increase the redshift, the upper bound as well as the instability gap increase similar to mass accretion rate.

filament temperature of around  $10^4\text{K}$ , below which there is no cooling. The right intersection point between  $\gamma_{\text{eff}} = 1.25$  and the calculated curve denotes the point where the cooling rate has gone down without any line cooling beyond  $10^5\text{K}$  and occurs at higher masses for higher accretion rates. The increase in the upper boundary of the instability gap can change by 2 orders of magnitude due to mass accretion rate. We find that lower mass accretion rates, in addition to having narrower instability gaps, lead to less of an overall dip in  $\gamma_{\text{eff}}$ .

Changing the time scale also affects the hydrodynamic instability gap as shown in Fig. 5. Larger redshifts lead to wider mass instability gaps with deeper dips. As with the mass accretion rates, the lower limit to the instability region remains largely unchanged; the upper mass limit grows significantly larger. We take a closer look at right boundary points as a function of the mass accretion rate, stratifying by redshift in Fig. 6. Increasing either the mass accretion rate or the redshift increases the prefactor of the cooling function,  $r\rho^2/pv$ . This scales the value of  $\gamma_{\text{eff}}$  downward for all mass ranges. This results in mainly increasing the upper critical value of  $M_{\text{fil}}$ , while the lower value stays relatively constant. The difference in the behavior arises because at low temperature around  $10^4\text{K}$ , the cooling function abruptly increases by orders of magnitude resulting in rapid decrease while at higher temperature around  $10^5\text{K}$  the change is smoother and the effect of prefactor becomes prominent.

Next, we determine whether the shock will be stable at an inner radius if it is not stable at the self-similar shock radius and starts to collapse. **DN: This sentence need rewriting.** Thus, we determine the shock stability condition at  $r < R_{\text{fil}}$ . To explore this we have to violate the self-similar assumption of a unique shock radius. We now assume that the shock jump occurs at radius  $r$  after following the collisionless solution for  $r' > r$ . We follow the same method to calculate the effective polytropic index as a function of mass, redshift, mass accretion rate, and radius.

The resulting  $\gamma_{\text{eff}}$  is visualized in Fig. 7 for  $s = 5$  at

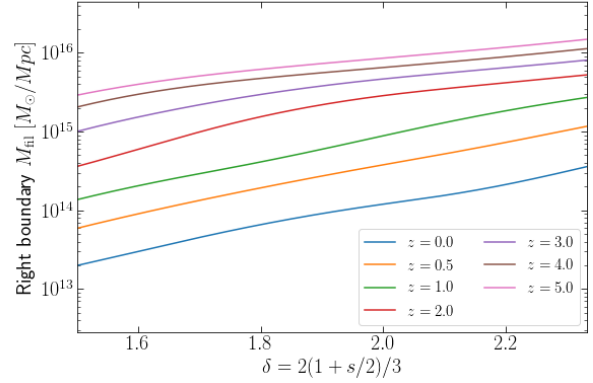


**Figure 6.** Right boundary in the mass instability gap, by redshift and accretion rate. The critical value increases with both mass accretion rate and redshift due to the overall decrease in  $\gamma_{\text{eff}}$  value.

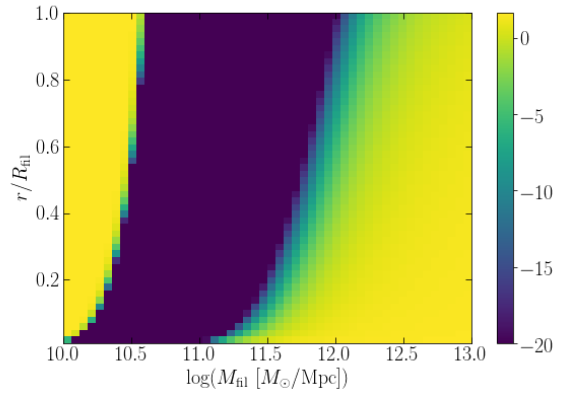


**Figure 7.** Heatmap of  $\gamma_{\text{eff}}$  for  $\gamma = 5/3$ ,  $z = 0.2$ , and  $s = 5$ . Only  $r/R_{\text{fil}} = 1$  is consistent with self-similarity.

$z = 0.2$ . As the radius decreases, the infall velocity increases, and resulting temperature inside the shock also increases without changing the overall magnitude. Thus, the instability gap just generally shifts to the left. This means that for some mass ranges, even though the shock is unstable at the location predicted by the self-similar solution, the collapse will stop at the inner radius. However, the shock radius started out at the self-similar predicted radius for  $M_{\text{fil}} = 10^{10} M_{\odot}/\text{Mpc}$  will not collapse, so the instability for shock at the inner radii should not matter. We note that the unstable shock will generally be halted at some inner radii for about half a dex of the upper critical point as shown in the previous section.

### 3.3 Shock and splashback radius

Based on our results from self-similar secondary accretion model and stability of shock due to cooling, we can predict the location of accretion shock radius of filaments with respect to the dark matter splashback. The shock ra-

dius of the filament is the radius identified by the self-similar solution if the cooling is not strong enough to collapse the shock at the self-similar defined shock. If the cooling causes the shock to be unstable, we define the maximum radius at which  $\gamma_{\text{eff}} > 1.25$  as the new shock radius. Figure 8 shows the mass per unit length of the filament vs the positions of shock and the splashback radii at different redshifts. At large mass per unit length, the log of mass per unit length is linearly proportional to the splashback radius of the filament. This trend agrees with the previous measurements in the dark matter only numerical simulations, but the proportionality constant is off due to different radius definitions we use and the filament finder algorithm defines (Cautun et al. 2014). The shock radius follows the same trend as the splashback radius, but quickly goes to 0 as the mass per unit length drops below the higher critical point into the unstable regime due to cooling.

Figure 9 highlights the ratio  $r_{\text{sh}}/r_{\text{sp}}$  as a function of filament mass with cooling. The ratio is close to 1 where the cooling is not strong, similar to the shock and splashback radius of halos (XS16). For very small and very large filament mass per unit length, the ratios with and without cooling are the same. In the middle is the gap where the shock is unstable and quickly decreases to zero, but the location of the splashback is unaffected. The drop at the low mass end is abrupt, while the drop at high mass end is slightly smoother due to the smooth cooling curves at high temperature as we have explored.

#### 4 DISCUSSION

In this section, we discuss several caveats and simplifying assumptions of our model and implications of our results.

When deriving the critical value of  $\gamma_{\text{eff}}$ , hydrostatic assumption is made (eq. 9). Self-similar solutions suggest this is not technically correct as there is small velocity even after shock (eq. 14 and Fig. 2). However, the resulting velocity is only about 10% of infall velocity outside the accretion shock and thus, the kinetic energy of gas is only 1% of thermal energy, and can indeed be neglected. However, filaments are not usually in hydrostatic equilibrium, but rather in hydrodynamic equilibrium. Turbulence generated by the accretion and vorticity around the filament due to collapsing sheets can contribute significant non-thermal pressure support (Codis et al. 2012, 2015; Laigle et al. 2015). If we assume that these additional pressures are subsonic after the accretion shock, the pressure support can be reduced by upto 50%. **DN: Where did this value come from? Need justification. Can we estimate this using analytic model of turbulent gas generation by Shi+14/Green+20? Such calculation is likely essential for comparing and understanding the simulated profiles that we plan to include in this paper.** Thus, we recalculate  $\gamma_{\text{eff}}$  for different redshifts as a function of mass per unit length when the thermal pressure  $p_{\text{th}} = \rho N_A k_B T$  is only 50% of the self-similar pressure which results in 50% of the temperature. As shown in fig. 10, this shifts the instability regime to higher mass values across the range due to the decrease in temperature for the same mass.

As noted before, we assume primordial composition for the metallicity of the gas, and thus, the cooling is dominated by hydrogen and helium cooling at  $10^4$  and  $10^5$  K

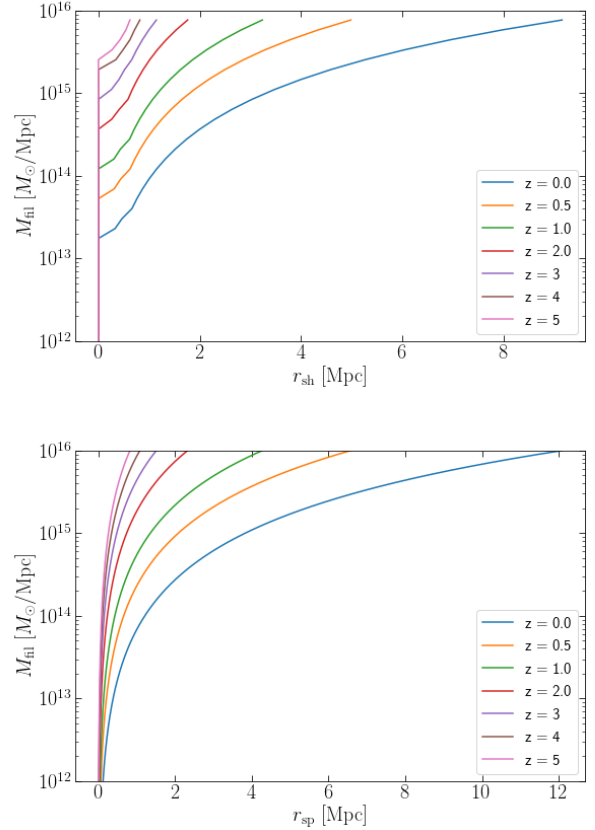


**Figure 8.** Mass per unit length of the filament vs the position of shock radius and the splashback radius for  $\gamma = 5/3$ . The two show similar trend where the log of mass per unit length is linearly proportional to the radius of the filament. The shock radius is cut off after certain mass per unit length due to cooling.

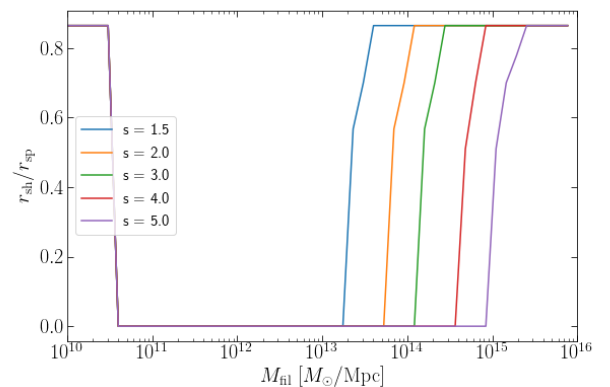


**Figure 9.** Position of shock radius with respect to splashback radius for  $\gamma = 5/3$ . For very low and very high mass per unit length, the two radii are very close to each other. In the middle, there is a region around which the shock radius will be much smaller than splashback.

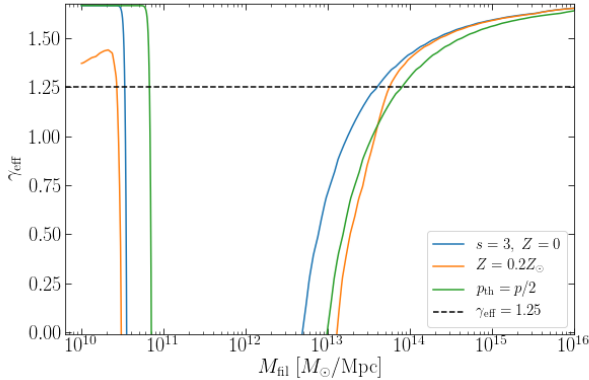


**Figure 10.** Gamma effective for different metallicity  $Z = 0.2$  and thermal pressure fraction  $p_{\text{th}} = 0.5p$ . Compared against baseline  $s = 3$ ,  $Z = 0$ , and  $z = 0$ .

respectively. However, the gas inside shock radius after the shock can mix with the high metallicity gas pushed out by the stellar feedback. The high metallicity gas is seen in the simulated halos out to  $r_{200\text{m}}$  (Biffi et al. 2017, 2018), and in observed filaments (Aracil et al. 2006). Thus, although there is no constrain on the metallicity of filament gas near shock, we can safely assume that the gas at shock will have less metallicity than that at  $r_{200\text{m}}$ . Fig. 10 shows that with higher metallicity  $Z = 0.2Z_{\odot}$ , the upper limit of the unstable regime generally increases due to increased line cooling by heavier elements.

Even though the self-similar models have been successful in predicting the splashback radius of the halo, it fails to correctly predict the density profile of dark matter halos. The density profile of halos in the numerical simulations is normally approximated as Navarro-Frenk-White profile with changing density slopes (Navarro et al. 1996) and deviates from the constant slope of the self-similar solution. This is because the density slope of self-similar solution depends on mass accretion rate (FG84), and changing mass accretion rate in the simulations helps shape the profile (Ludlow et al. 2013). However, filament profile does not depend on mass accretion rate as shown here and in FG84. Hence we predict the density profile of the filament model to be more robust compared to the halo model.

Note that our model is built upon EdS universe, instead of the concordance  $\Lambda$ CDM model. **DN: Calculations based on EdS is a useful academic exercise, but  $\Lambda$ CDM calculations are required along with rigorous comparisons to simulation measurements, if this work were to be published in a professional journal.** Reducing  $\Omega_m$  from 1 to 0.3 at observed time usually results in higher overdensity by a factor of 2–4 (Adhikari et al. 2014; Shi 2016a). As shown in eq. 13, the temperature of the filament only depends on the mass per unit length of the filament, and have no dependence on mass accretion rate or background density. Thus, assuming that the change in shock radius of filament is the same as the change in splashback radius of halo, switching to  $\Lambda$ CDM increases the prefactor  $r\rho^2/pv$  upto a factor of 2 further increasing the dip of  $\gamma_{\text{eff}}$ , without altering the cooling curve.

Thus, it simply increases the upper limit of instability regime slightly.

In addition, the model simplifies the filamentary gas stream by assuming infinite cylinder with no flow. These assumptions are only applicable to the regions of filament far from the end where they connect to the halos. Near the end, filaments have velocity along the axis into the halos, and the axis is not infinite. However, the self-similar solution is invariant along the axis. Thus, our solutions still serve as the first order solution and we expect the corrections from these effects to be minor far from the halos. Recent numerical studies have also shown that the splashback radius of the halo determined from density profile may not represent the edge of the entire phase space of the halo (Aung et al. 2020). This likely stems from the highly aspherical splashback surface (Mansfield & Kravtsov 2020). **DN: Not clear why this discussion is relevant for filaments. Establish more rigorous connection or remove this argument.** Our study also assumes perfect cylindrical symmetry for the filaments, which will likely break down for cosmological filaments. Upcoming simulations with increased resolution for low density regions and better filament identifiers will be useful in calibrating how robust the self-similarity assumptions are.

## 5 CONCLUSIONS

In this paper, we examine the stability of accretion shock around cooling filaments using a self-similar model, in which collisionless dark matter and collisional gas are modeled self-consistently using the secondary matter accretion model of a cylindrical filament. **DN: The conclusions come across overly qualitative and trivial. Report more quantitative results. Highlight novelties of the results more prominently.**

- The self-similar shock radius decreases as the mass accretion rate increases. The ansatz of self-similarity yields similar results for filaments as it does for halos, with some notable exceptions: the apocenters of dark matter trajectories grow over time for  $s < 2.5$ , and stable gas profiles cease to exist at  $s < 1$ . These differences can be attributed to the Hubble flow along the filament’s axis.
- Across all the mass accretion rates for which the self-similar solution is stable, we find close alignment between the dark matter splashback and shock radii. We found the density slope inside the filament to be  $\rho \propto r^{-1.6}$ , independent of mass accretion rate.
- We found that cooling can significantly disrupt the stability of the filaments by decreasing the temperature and pressure of the post-shock gas. The stability criterion depends on the mass accretion rate, mass per unit length and redshift of the filament. There is an instability gap in mass range within which radiative cooling can remove the pressure support for the shock. As the redshift and mass accretion rate increase, the mass instability gap also increases.
- Without cooling, shock radius is approximately at the location of splashback radius of the filament, similar to the results of the halos. However, due to the effects of cooling, the shock radius can significantly be smaller in certain range of mass per unit length.

The baryonic gas in the filaments can account for missing baryons in universe and contribute to biases if the



gas signal is assumed to come from halos only (Hallman et al. 2007; Planck Collaboration et al. 2013; Akamatsu et al. 2017). Further understandings of gas filaments require studying the gas filaments in hydrodynamical cosmological simulations. Recent developments in simulations and filament identification algorithms (e.g. Sousbie 2011; Cautun et al. 2013; Pereyra et al. 2019) have allowed us to probe dark matter filaments. Calibration of dark matter profiles with the numerical simulations will allow us to understand and relax the self-similar assumptions and identify how accurate the secondary accretion model is. Future hydrodynamical simulations with or without cooling and feedback should advance our understandings of the filaments as well as connection to the growth of halos they feed. With next generation surveys that can probe into gaseous filaments such as Simons Observatory (Suzuki et al. 2016) and CMB-S4 (Abazajian et al. 2016), the signals from these filaments can be detected. Our model provides an important first step in theoretical modeling of filaments and allows us to model the gas in filaments expected to be detected in the next decades.

## REFERENCES

- Abazajian K. N., et al., 2016, preprint, ([arXiv:1610.02743](https://arxiv.org/abs/1610.02743))  
 Adhikari S., Dalal N., Chamberlain R. T., 2014, *J. Cosmology Astropart. Phys.*, 2014, 019  
 Akamatsu H., et al., 2017, *A&A*, 606, A1  
 Aracil B., Tripp T. M., Bowen D. V., Prochaska J. X., Chen H.-W., Frye B. L., 2006, *MNRAS*, 367, 139  
 Aung H., Cohn J. D., 2016, *MNRAS*, 456, 909  
 Aung H., Nagai D., Rozo E., Garcia R., 2020, arXiv e-prints, p. [arXiv:2003.11557](https://arxiv.org/abs/2003.11557)  
 Bertschinger E., 1985, *ApJS*, 58, 39  
 Biffi V., et al., 2017, *MNRAS*, 468, 531  
 Biffi V., Planelles S., Borgani S., Rasia E., Murante G., Fabjan D., Gaspari M., 2018, *MNRAS*, 476, 2689  
 Birnboim Y., Dekel A., 2003, *MNRAS*, 345, 349  
 Birnboim Y., Padnos D., Zinger E., 2016, *ApJ*, 832, L4  
 Bregman J. N., 2007, *ARA&A*, 45, 221  
 Cautun M., van de Weygaert R., Jones B. J. T., 2013, *MNRAS*, 429, 1286  
 Cautun M., van de Weygaert R., Jones B. J. T., Frenk C. S., 2014, *MNRAS*, 441, 2923  
 Cen R., Ostriker J. P., 1999, *ApJ*, 514, 1  
 Ceverino D., Dekel A., Bournaud F., 2010, *MNRAS*, 404, 2151  
 Codis S., Pichon C., Devriendt J., Slyz A., Pogosyan D., Dubois Y., Sousbie T., 2012, *MNRAS*, 427, 3320  
 Codis S., Pichon C., Pogosyan D., 2015, *MNRAS*, 452, 3369  
 Davé R., et al., 2001, *ApJ*, 552, 473  
 Dekel A., et al., 2009, *Nature*, 457, 451  
 Doroshkevich A. G., 1970, *Astrophysics*, 6, 320  
 Fillmore J. A., Goldreich P., 1984, *ApJ*, 281, 1  
 Hahn O., Porciani C., Carollo C. M., Dekel A., 2007, *MNRAS*, 375, 489  
 Hallman E. J., O’Shea B. W., Burns J. O., Norman M. L., Harkness R., Wagner R., 2007, *ApJ*, 671, 27  
 Hernández-Monteagudo C., Ma Y.-Z., Kitauro F. S., Wang W., Génova-Santos R., Macías-Pérez J., Herranz D., 2015, *Phys. Rev. Lett.*, 115, 191301  
 Kereš D., Katz N., Weinberg D. H., Davé R., 2005, *MNRAS*, 363, 2  
 Laigle C., et al., 2015, *MNRAS*, 446, 2744  
 Lim S. H., Mo H. J., Wang H., Yang X., 2020, *ApJ*, 889, 48  
 Ludlow A. D., et al., 2013, *MNRAS*, 432, 1103

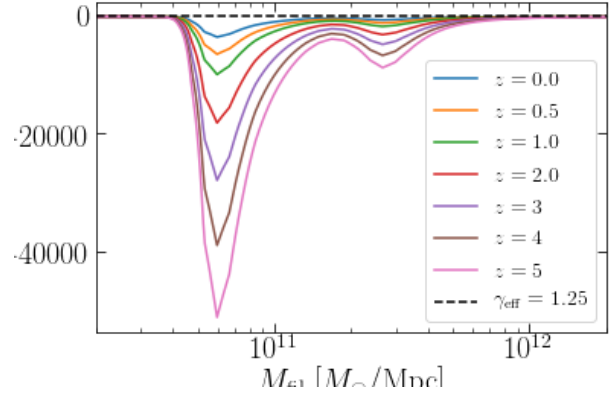


**Figure B1.**  $\gamma_{\text{eff}}$  values at  $r = R_{\text{fil}}$  for different redshifts.

- Mansfield P., Kravtsov A. V., 2020, *MNRAS*, 493, 4763  
 Navarro J. F., Frenk C. S., White S. D. M., 1996, *ApJ*, 462, 563  
 Nicastro F., et al., 2018, *Nature*, 558, 406  
 Pereyra L. A., Sgró M. A., Merchán M. E., Stasyszyn F. A., Paz D. J., 2019, arXiv e-prints, p. [arXiv:1911.06768](https://arxiv.org/abs/1911.06768)  
 Planck Collaboration et al., 2013, *A&A*, 550, A134  
 Shi X., 2016a, *MNRAS*, 459, 3711  
 Shi X., 2016b, *MNRAS*, 461, 1804  
 Sousbie T., 2011, *MNRAS*, 414, 350  
 Sutherland R. S., Dopita M. A., 1993, *ApJS*, 88, 253  
 Suzuki A., et al., 2016, *Journal of Low Temperature Physics*, 184, 805  
 Tanimura H., Aghanim N., Bonjean V., Malavasi N., Douspis M., 2019, arXiv e-prints, p. [arXiv:1911.09706](https://arxiv.org/abs/1911.09706)  
 Zinger E., Dekel A., Birnboim Y., Kravtsov A., Nagai D., 2016, *MNRAS*, 461, 412  
 de Graaff A., Cai Y.-C., Heymans C., Peacock J. A., 2019, *A&A*, 624, A48

## APPENDIX A: FILAMENT VIRIAL OVERDENSITY

Derive similar overdensity definition like B&M form cylindrical collapse. Add a plot using radius overdensity vs mass overdensity

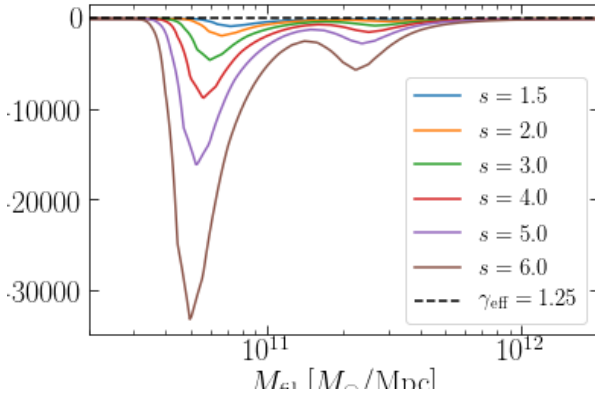
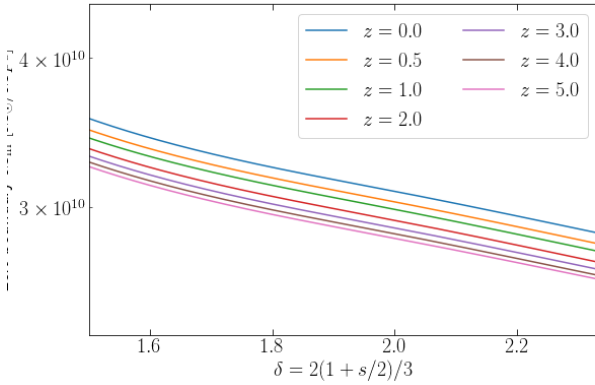
## APPENDIX B: NEGATIVE $\gamma_{\text{EFF}}$

Should be removed. Keeping here just in case.

## APPENDIX C: EXACT MASS VALUES

Should be removed. Keeping here just in case. The lower and upper bound values in table C1

$\gamma =$	5/3		2		7/3	
$z$	L.B.	U.B.	L.B.	U.B.	L.B.	U.B.
0.0	$2.65 \cdot 10^{10}$	$7.7 \cdot 10^{12}$	$2.67 \cdot 10^{10}$	$3.54 \cdot 10^{13}$	$2.63 \cdot 10^{10}$	$1.62 \cdot 10^{14}$
0.1	$2.78 \cdot 10^{10}$	$1.25 \cdot 10^{13}$	$2.79 \cdot 10^{10}$	$6.41 \cdot 10^{13}$	$2.74 \cdot 10^{10}$	$3.07 \cdot 10^{14}$
0.2	$2.91 \cdot 10^{10}$	$1.15 \cdot 10^{14}$	$2.82 \cdot 10^{10}$	$6 \cdot 10^{14}$	$2.63 \cdot 10^{10}$	$2.92 \cdot 10^{15}$
0.3	$3.03 \cdot 10^{10}$	$3.59 \cdot 10^{13}$	$3.01 \cdot 10^{10}$	$1.23 \cdot 10^{15}$	$2.67 \cdot 10^{10}$	$4.38 \cdot 10^{15}$
0.4	$3.15 \cdot 10^{10}$	$6.13 \cdot 10^{13}$	$3.10 \cdot 10^{10}$	$4.15 \cdot 10^{14}$	$2.95 \cdot 10^{10}$	$2.66 \cdot 10^{15}$
0.5	$3.26 \cdot 10^{10}$	$1.08 \cdot 10^{14}$	$3.18 \cdot 10^{10}$	$8.26 \cdot 10^{14}$	$2.99 \cdot 10^{10}$	$4.61 \cdot 10^{15}$

**Table C1.** Lower and Upper bound of instability regimes for filaments**Figure B2.**  $\gamma_{\text{eff}}$  values at  $r = R_{\text{fil}}$  for different mass accretion rates. The dips are largely due to the shape of the cooling function.**Figure B3.** Left boundary in the mass instability gap, by redshift and accretion rate